



Reduced mixing in inertial confinement fusion with early-time interface accelerationC. R. Weber, D. S. Clark, D. T. Casey, G. N. Hall, O. Jones, O. Landen , A. Pak, and V. A. Smalyuk
Lawrence Livermore National Laboratory, P.O. Box 808, Livermore, California 94551-0808, USA (Received 30 June 2023; accepted 24 July 2023; published 16 August 2023)

In inertial confinement fusion (ICF) implosions, the interface between the cryogenic DT fuel and the ablator is unstable to shock acceleration (the Richtmyer-Meshkov instability, RM) and constant acceleration (Rayleigh-Taylor instability, RT). Instability growth at this interface can reduce the final compression, limiting fusion burnup. If the constant acceleration is in the direction of the lighter material (negative Atwood number), the RT instability produces oscillatory motion that can stabilize against RM growth. Theory and simulations suggest this scenario occurred at early times in some ICF experiments on the National Ignition Facility, possibly explaining their favorable performance compared to one-dimensional simulations. This characteristic is being included in newer, lower adiabat designs, seeking to improve compression while minimizing ablator mixing into the fuel.

DOI: [10.1103/PhysRevE.108.L023202](https://doi.org/10.1103/PhysRevE.108.L023202)

To ignite and burn an inertial confinement fusion (ICF) [1,2] target, the deuterium-tritium (DT) fuel must be compressed to high areal densities to confine the hot spot and give time for fusion alpha particles to heat and bootstrap the ignition process. Experience with ICF designs on the National Ignition Facility (NIF) [3–5] that use high-density carbon (HDC) [6,7] (diamond) ablaters has, however, not shown the expected compression increase between designs that seek to lower the entropy of the fuel [8]. A possible reason is due to mixing at the fuel-ablator interface [9–11], which can heat the fuel, increase its entropy, limit the final compression, and ultimately reduce the fuel burnup. In this work we show a stabilizing mechanism that may have aided the compression of some ICF designs: an interface experiencing constant acceleration following the shock breakout can have significantly less perturbation growth than without this acceleration. Designs that incorporate this technique can potentially improve compression while minimizing ablator mixing into the DT fuel, allowing for higher target gains to be achieved.

In ICF, the laser pulse is tailored to send a series of shock waves to compress the cryogenic deuterium-tritium (DT) fuel. Since an individual shock wave can only compress the fuel by up to $4\times$ from its initial 0.25 g/cm^3 , separating the shocks into—two to four carefully timed shocks can combine for a larger compression [12]. Unexpectedly, however, two designs frequently used on NIF that have two or three shocks crossing through the ice exhibit very similar levels of compression [8]. These designs are shown in Fig. 1. Both designs use an HDC ablator and have three steps in the laser pulse, sending three shock waves. Typical shock timing is used in the “HDC” design with the three shocks timed to traverse the cryogenic DT ice separately before merging near the ice-gas interface [11,13]. This shock-timing strategy is the same as used in the larger-scale “Hybrid-E” design that achieved a burning and igniting plasma [14–18]. The “Big-foot” design [19–21] deliberately merges the first two shocks prior to their reaching the ice, so the ice only senses two shocks, the first one very strong, and is therefore on a higher adiabat (where adiabat is the ratio of the pressure to the Fermi degenerate pressure

[22] and is a measure of the fuel’s entropy). Implosions with a lower adiabat (entropy) following the shock traversals can compress greater during the final stagnation phase. Simulations expect the HDC design to have an adiabat of 3 at the time of peak implosion velocity, while the Big-foot design’s adiabat is 4.2. In experiments, the compression of the fuel is measured by the down-scattered ratio (DSR) of scattered-to-primary DT fusion neutrons and is approximately related to the fuel areal density by $\rho R_{\text{fuel}} \approx 19\text{ DSR}$. This DSR was simulated to be 3.9% for HDC and 3.2% for Big-foot, but both experiments recorded $3.1 \pm 0.2\%$ (NIF experiments N170827 and N180128).

A possible reason for the reduced compression in the HDC design is material mixing at the fuel-ablator interface. Mixing of ablator material into the dense DT fuel will heat the fuel, increasing its entropy and reducing its final compression [9,11,23,24]. This picture is supported by high-resolution two-dimensional (2D) simulations. Figure 2 shows simulations using Hydra [25] to model an 8° wedge at the equator with 0.004° resolution and includes surface roughness and a model of HDC’s microstructure [26,27]. This simulation assumed an HDC grain size of 2 microns and deresolved the 4-nm interstitials to 200 nm, conserving mass, but may underpredict the full extent of the mixing [28,29]. These simulations are near the time of peak fuel velocity at radius 200 micron (convergence ratio ~ 4.5), prior to the stagnation shock slowing down the shell. The HDC design experiences fine-scaled mixing of ablator material into the DT. As this hot carbon mix enters the ice, it locally heats the surrounding DT and lowers its density. In contrast, the Big-foot design has no fine-scale mixing occurring at this interface.

The impact of these levels of mixing on compression is estimated using 1D simulations with a “fall-line” mix model, which allows the mix level to be adjusted to account for higher amounts of mixing that may occur in experiments. This model does not produce a predictive level of mix, as the user needs to specify when mixing starts, and the simulation will then mix across the interface based on the distance it has accelerated beyond its free-fall location. In this configuration, we are

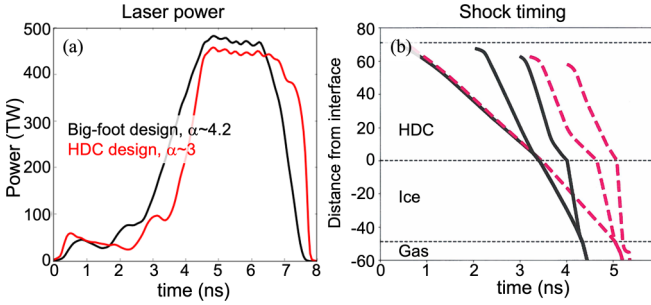


FIG. 1. (a) Laser pulse history and (b) shock wave trajectory in Lagrangian coordinates for the Big-foot and HDC designs. Both designs have three shocks but in the Big-foot design the first two shocks are timed to merge prior to entering the ice, increasing the entropy of the fuel. The final shock is designed to merge near the ice-gas interface.

mixing during the in-flight acceleration period, rather than the late-time deceleration period used by others [30]. This model, in its implementation in Hydra, runs in-line, mixing materials and updating the equation of state as the simulation evolves, but the mixing does not respond dynamically to these changes, as the mix width is solely prescribed by the fall-line distance. Other models, like RANS-based models [31–33] or buoyancy-drag models [34–36], can dynamically respond based on local changes to the Atwood number or sound speed. Figure 2(c) shows simulations with mixing turned on at various times, finding compression dropping for both designs as the fuel-ablator mix width is increased. The mix width in this figure is measured at the time of peak velocity, 7.80 ns for HDC and 7.60 ns for Big-foot. At ~20 microns of mix width [similar to that seen in Fig. 2(b)], the DSR drops to 80%

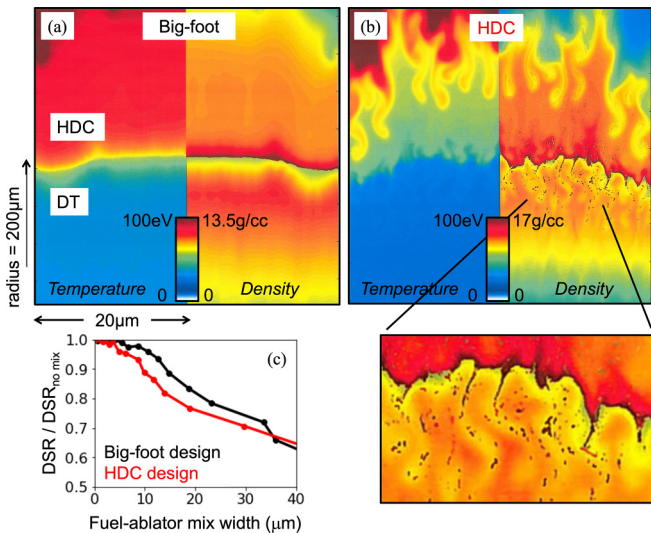


FIG. 2. Density and temperature at the fuel-ablator interface in high-resolution 2D simulations at radius 200 microns in the (a) Big-foot and (b) HDC designs. Times are 7.50 and 7.68 ns for (a) and (b). Big-foot appears very stable at this interface while with the HDC design there is ablator material mixing into the DT fuel. The impact of mix on DSR is shown in (c) from 1D simulations with an in-flight fall-line mix model turned on at various times.

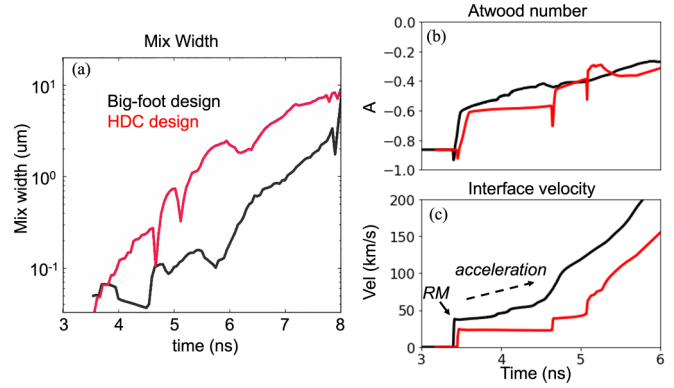


FIG. 3. (a) Mix width from the simulations in Fig. 2. The mix width is the extent that ablator material goes from 0.1% to 99.9% at the fuel-ablator interface. (b) Atwood number vs time and (c) fuel-ablator interface velocity. The difference in mix width is apparent immediately and appears to be due to the initial RM growth, as during this time the Atwood numbers are negative (stable) for both designs. The main difference is that there is a near constant acceleration in the Big-foot design following the initial shock breakout.

of its original value for both designs. Interestingly the HDC design is degraded more for a given level of mix because the lower adiabat results in a thinner fuel layer at peak velocity (25 microns vs 39 microns for Big-foot), thus more of the fuel is contaminated.

The traditional view of stability at this interface has been related to the classical Rayleigh-Taylor (RT) instability [37–40], where mixing would occur if the HDC ablator were lower density than the DT fuel in-flight, but these simulations suggest these densities are very similar and a different mechanism is responsible for the mixing dynamics.

To understand the cause of the mix-width difference between these two designs, we look at the time history of the mixing layer, shown in Fig. 3. The mix widths of these two designs diverge immediately following shock breakout at 3.4 ns. At this early time, the interface is stable to Rayleigh-Taylor growth, as shown in Fig. 3(b), due to its negative Atwood number [$A = (\rho_{abl} - \rho_{DT}) / (\rho_{abl} + \rho_{DT})$], comparing the density between the ablator and DT]. Both designs experience an impulsive acceleration which will lead to growth from the Richtmyer-Meshkov (RM) instability [41,42], but we see in Fig. 3(c) that the Big-foot design is further accelerating following the shock breakout whereas the HDC design has a constant velocity. This acceleration difference appears to be the cause of the mix-width divergence.

The impact of constant interface acceleration following the impulsive RM growth can be understood by considering the dispersion equation for an interface perturbation of height h and frequency $\gamma^2 = Agk$, where g is the acceleration and k is the wave number [43]:

$$\frac{\partial h^2}{\partial t^2} - \gamma^2 h = 0. \tag{1}$$

For a constant γ this has the solution

$$h(t) = h_0 \cosh(\gamma t) + \frac{\dot{h}_0}{\gamma} \sinh(\gamma t). \tag{2}$$

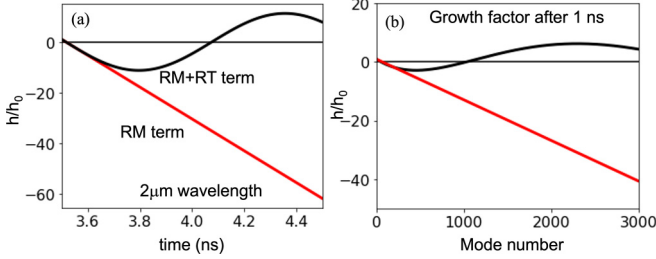


FIG. 4. (a) Interface growth vs time following a Richtmyer-Meshkov (RM) interaction (red) or RM followed by Rayleigh-Taylor (RT) acceleration. The acceleration imparts an oscillation, limiting the unbounded RM growth. (b) Growth factor after 1 ns for a spectrum of mode numbers. Above mode 200 the growth factor is reduced with the acceleration term, with a zero near mode 1000.

When $Agk < 0$, like the initial stage of these designs, where the ablator is much denser than the DT fuel, this equation has oscillatory sine and cosine solutions,

$$h(t) = h_0 \cos(\gamma t) + \frac{\dot{h}_0}{\gamma} \sin(\gamma t). \quad (3)$$

The initial growth rate can be approximated by the impulsive RM formula $\dot{h}_{0, \text{RM}} = \nabla V A k h_0$, where ΔV is the jump in interface velocity caused by the shock. Using the values similar to Fig. 3, $A = -0.5$, $g = 20$ micron/ ns^2 , and a 2-micron wavelength, Figure 4 shows the time history expected for a perturbation with and without a constant acceleration following the RM impulse of $\dot{h}_0/h_0 = -63 \text{ ns}^{-1}$. The oscillatory behavior of the constant acceleration limits the RM growth to a maximum amplitude of $h_0 \sqrt{1 + \Delta V^2 A k / g}$. Figure 4(b) shows the growth factor (h/h_0) after 1 ns following the initial shock acceleration for a range of mode numbers (k^* radius). This is approximately the time the second shock wave arrives, which will amplify any perturbations that grown during the first phase. The growth factor of low mode numbers is relatively unchanged, but by mode 200 the growth starts to reduce and inverts by mode 1000, with another inversion occurring at higher modes. This picture suggests that designs can aim to place the growth factor zero at the most dangerous mode, for example ablators like HDC and Be that have crystalline structure can time the growth factor at the grain scale to be zero when the second shock arrives. The 2-micron grain scale used in the simulations of Fig. 2 induce a mode ~ 3000 perturbation, nearing one of the zeros in this growth-factor curve. The stabilizing effect that RT can have on RM has been recognized elsewhere, particularly in experiments that are trying to achieve pure RM but must account for acceleration effects [44–48].

We performed 2D ICF implosion simulations with single-mode perturbations to test this predicted oscillatory behavior in this more complicated scenario with time-varying accelerations and densities. These calculations impose a very small (0.01 nm) sine-wave perturbation at the fuel-ablator interface and track its amplitude growth through time. To analytically compute the RM growth rate, the impulsive growth-rate formula of Ref. [49] was used, which incorporates compressibility effects by averaging the post- (+) and preshock (-) A

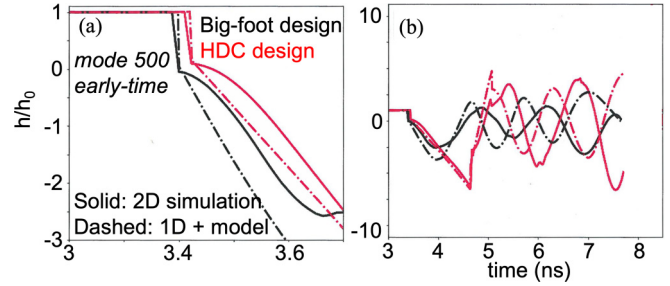


FIG. 5. Growth factors from a mode 500 simulation (a) at early time and (b) up until peak velocity. At early time, the model accurately reproduces the compression and the growth rate, though sound-speed effects in the 2D simulation cause some delay that impacts the phase later in time. The model predicts a similar amplitude later in time, showing that mode 500 growth is minor at this interface.

and h ,

$$\frac{dh}{dt} = \frac{1}{2} k \Delta V (A^+ h_0^+ + A^- h_0^-).$$

The postshock amplitude is computed per Ref. [41] by noting that the shock of speed U_s will reach the peak of the perturbation first, accelerating it to a velocity of ΔV over a time h_0/U_s before reaching the trough. Therefore, the amplitude will reduce to

$$h_0^+ = h_0^- \left(1 - \frac{\Delta V}{U_s} \right).$$

The pre and post-shock Atwood numbers are computed through 1D simulations as shown in Fig. 3. To combine RM and RT effects in our analytical expression, Eq. (1) is augmented as

$$\frac{d^2 h}{dt^2} = \begin{cases} \frac{1}{2} k \Delta V (A^+ h_0^+ + A^- h_0^-) \delta(t) & \text{RM} \\ \gamma^2 h & \text{RT} \end{cases}, \quad (4)$$

where the RM acceleration term is used if large interface accelerations are detected. For simplicity, this analysis omits Bell-Plessett [50,51] effects, which can become important at late times. This equation is numerically integrated from the 1D simulations. Figure 5(a) shows this analytical model compared to the 2D perturbation simulation during the initial RM interaction. The interface amplitude compresses by $\sim 10\times$ and then grows in the negative direction. This 1D model accurately reproduces the growth rate, but the 2D simulations show a startup delay before reaching their linear rate. This delay is due to the finite time (wavelength/sound speed) required for the baroclinic vorticity to communicate with the peak and trough of the perturbation [52]. One could add this delay time to this model, but it adds more complexity and is not needed for higher modes. Figure 5(b) shows that later in time, this simple model has approximately reproduced the amplitude and periodicity of this mode 500 perturbation, but small differences have accumulated and the two curves are out of phase. At this mode number the two designs show a similar growth factor of 3–6 \times . This level of growth is minor given the submicron perturbations present on these capsules.

At high mode numbers, where the RM growth is larger but the oscillatory impact of the RT term can reduce the overall growth, these two designs have significantly different growth

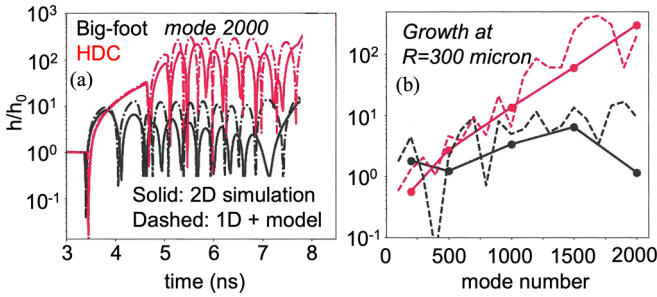


FIG. 6. Growth factor (h/h_0) (a) vs time at mode 2000 and (b) vs mode number. The model reproduces the observed behavior, where the HDC design (red) shows significantly more growth than Big-foot (black) at modes above 1000.

factors. Figure 6(a) shows a 2D simulation with a linear mode 2000 perturbation compared to this analytical model. The model again does a good job at matching the early-time growth, the periodicity, and the approximate magnitude, but some small differences again accumulate. At late times (7–8 ns), the growth factors of these two designs differ by $\sim 20 - 50\times$. Despite the detailed differences between the model and the 2D simulation, it is clearly useful for differentiating designs that will incur high-mode growth from those that remain stable [Fig. 5(d)]. The computed cost of this model from a 1D simulation is $\sim 10^{-5}\times$ less than the 2D simulation shown in Fig. 2, so there is clear value in using this when doing initial design scoping. The growth factor spectrum [Fig. 6(b)] using this model compared to a set of 2D calculations both show a similar picture as our simple estimate from Fig. 2, where the stabilization from RT keeps the Big-foot growth factors low.

To predict the mix width, the growth-factor estimations from this model need to be combined with the seeds on the capsule. While the roughness of many ablators is small at the very-high wave numbers that are considered here, internal or isolated defects can imprint perturbations on the interface at all mode numbers. The typical concern with isolated defects is that they can inject a jet into the hot spot [53,54], but if there are significant numbers of them, like with HDC’s microstructure, they can couple to high modes and the mechanisms discussed here can contribute to fuel-ablator mixing. Once the growth becomes nonlinear ($kh \sim 1$) mode-coupling, bubble-merger, and other mechanisms will come into play, changing the growth rate from these linear predictions [55–58].

The reason for the initial accelerating interface in the Big-foot pulse is explored in Fig. 7, showing four pressure profiles as the shocks move through the ablator four times. In the first three times we see the first shock with a flat ~ 11 Mbar pressure profile behind it. Shock 2, however, is followed by a steep gradient in pressure. This is due to the radiation drive history: despite the near flat laser power in the second pulse (2–3 ns), the radiation temperature is increasing in time as the hohlraum albedo is increasing as energy is stored in walls. Since the ablation pressure scales as $P_{abl} \propto T^{3.5}$, the rising ablation pressure will lead to a pressure gradient between the shock and the ablation front and will ultimately cause the interface to accelerate when shock 2 overtakes shock 1 before it breaks out into the DT ice.

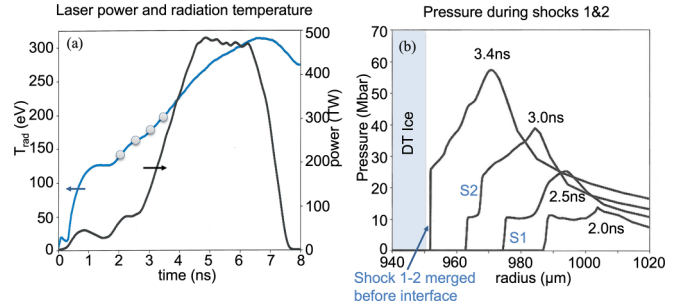


FIG. 7. (a) Radiation temperature and laser power history for the Big-foot design. (b) Pressure profiles at for times prior to the shock reaching the DT ice, with times also marked in (a). The first pulse as a flat T_r history and the shock has flat trailing pressure profile, but the second shock has a ramped trailing pressure profile, owing to the increasing T_r history in the drive. This pressure gradient is what causes the interface acceleration when the merged first and second shocks merge and accelerate the interface.

The ramped pressure profile of Fig. 7 gives guidance on how designs can seek a lower adiabat like HDC but retain the stabilizing characteristics of Big-foot. Two strategies are apparent: tailor the first shock so that it has an increasing pressure profile behind it to further accelerate the interface after breakout, or reduce the strength of the second shock in Big-foot but keep its pressure gradient and shock 1–2 merge time. The first strategy has the greatest potential, as a single shock can be near the limit of HDC’s melt pressure [59] and deposit less entropy than two shocks, but it is likely more difficult to achieve, as a time dependent laser profile will need to be specified to accelerate the interface in the presence of EOS and hohlraum-dynamics uncertainties. The current “SQ-n” campaign on NIF is including this technique and others in a focused effort to increase compression in HDC implosions with minimal instability growth [60] and its interface acceleration history is being measured using a refraction enhanced radiography technique [61]. Preliminary results of these experiments suggest that this strategy successfully improved the compression [62]. Figure 8 shows an example of the second strategy, where the drive flux in the second shock of Big-foot is reduced by $0.7\times$. The third shock is also delayed to preserve the shock-timing strategy, with shocks 1 and 2 still merging in the ablator and the third shock merging near the ice-gas

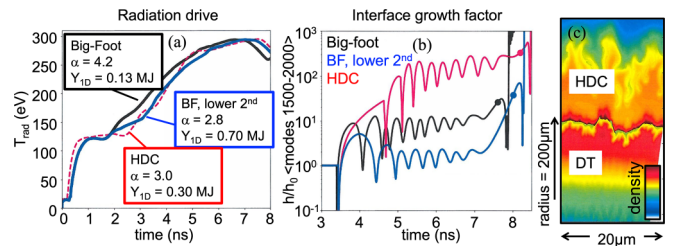


FIG. 8. (a) Radiation drive history including an improved design (blue) that lowers the second shock pressure but preserves its stabilizing characteristics. (b) The growth factors, averaged over modes 1500–2000, show similar stability as Big-foot. (c) A high-resolution 2D simulation shows that the interface is more stable than HDC (Fig. 2) and similar to Big-foot.

interface. This weaker merged shock reduced the adiabat of Big-foot from 4.2 to 2.8, increasing its 1D yield by $5\times$. The 1D stability metric is shown in Fig. 8(b), but to reduce the oscillations the growth factors for modes 1500–2000 are averaged. This shows that this Big-foot design with a lower second shock has better early-time stability than the original Big-foot design. Later in time at 8 ns, this modified design experiences more growth due to a slightly unstable Atwood number (0.07, vs 0.0 for Big-foot). This design did not change the capsule properties, which could be further optimized by increasing the dopant to improve the Atwood number. A high-mode simulation of this design, shown in Fig. 8(c), shows that the fuel-ablator mixing is similar to Big-foot and causes much less small-scale growth than in HDC.

In summary, the acceleration history of the fuel-ablator interface can be an important stabilizing lever, as it limits unbounded RM growth to an oscillatory behavior. This could have been responsible for the favorable performance of the Big-foot experiments compared to lower adiabat designs with conventional shock timing. Since designs with conventional shock timing continue to be used, delivering increased fusion output at a larger scale, this work suggests further improvements are possible by reducing the growth during the Richtmyer-Meshkov period. Future designs can specifi-

cally seek to impose an acceleration, through an increasing ablation-pressure history or through shock mergers as seen in the Big-foot design.

This work was performed under the auspices of the U.S. Department of Energy by the Lawrence Livermore National Laboratory under Contract No. DE-AC52-07NA27344. This document was prepared as an account of work sponsored by an agency of the United States government. Neither the United States government nor Lawrence Livermore National Security, LLC, nor any of their employees makes any warranty, expressed or implied, or assumes any legal liability or responsibility for the accuracy, completeness, or usefulness of any information, apparatus, product, or process disclosed, or represents that its use would not infringe privately owned rights. Reference herein to any specific commercial product, process, or service by trade name, trademark, manufacturer, or otherwise does not necessarily constitute or imply its endorsement, recommendation, or favoring by the United States government or Lawrence Livermore National Security, LLC. The views and opinions of authors expressed herein do not necessarily state or reflect those of the United States government or Lawrence Livermore National Security, LLC, and shall not be used for advertising or product endorsement purposes.

-
- [1] J. Lindl, Development of the indirect-drive approach to inertial confinement fusion and the target physics basis for ignition and gain, *Phys. Plasmas* **2**, 3933 (1995).
 - [2] S. Atzeni and J. Meyer-ter-Vehn, *The Physics of Inertial Fusion* (Oxford University Press, Oxford, 2004).
 - [3] G. H. Miller, E. I. Moses, and C. R. Wuest, The national ignition facility, *Opt. Eng.* **43**, 2841 (2004).
 - [4] E. I. Moses, R. N. Boyd, B. A. Remington, C. J. Keane, and R. Al-Ayat, The National Ignition Facility: Ushering in a new age for high energy density science, *Phys. Plasmas* **16**, 041006 (2009).
 - [5] M. L. Spaeth, K. R. Manes, D. H. Kalantar, and P. E. Miller, Description of the NIF Laser, *Fusion Sci. Technol.* **69**, 25 (2016).
 - [6] J. Biener *et al.*, Diamond spheres for inertial confinement fusion, *Nucl. Fusion* **49**, 112001 (2009).
 - [7] C. Dawodeit *et al.*, Grain size dependent physical and chemical properties of thick CVD diamond films for high energy density physics experiments, *Diamond Relat. Mater.* **40**, 75 (2013).
 - [8] O. L. Landen *et al.*, Fuel convergence sensitivity in indirect drive implosions, *Phys. Plasmas* **28**, 042705 (2021).
 - [9] B. A. Hammel *et al.*, High-mode Rayleigh-Taylor growth in NIF ignition capsules, *High Energy Density Phys.* **6**, 171 (2010).
 - [10] C. R. Weber *et al.*, First Measurements of Fuel-Ablator Interface Instability Growth in Inertial Confinement Fusion Implosions on the National Ignition Facility, *Phys. Rev. Lett.* **117**, 075002 (2016).
 - [11] L. Berzak Hopkins *et al.*, Increasing stagnation pressure and thermonuclear performance of inertial confinement fusion capsules by the introduction of a high-Z dopant, *Phys. Plasmas* **25**, 080706 (2018).
 - [12] D. H. Munro *et al.*, Shock timing technique for the National Ignition Facility, *Physics of Plasmas (1994-present)* **8**, 2245 (2001).
 - [13] S. Le Pape *et al.*, Fusion Energy Output Greater Than the Kinetic Energy of an Imploding Shell at the National Ignition Facility, *Phys. Rev. Lett.* **120**, 245003 (2018).
 - [14] A. L. Kritcher *et al.*, Achieving record hot spot energies with large HDC implosions on NIF in HYBRID-E, *Phys. Plasmas* **28**, 072706 (2021).
 - [15] A. L. Kritcher *et al.*, Design of inertial fusion implosions reaching the burning plasma regime, *Nat. Phys.* **18**, 251 (2022).
 - [16] H. Abu-Shawareb *et al.* (Indirect Drive ICF Collaboration), Lawson Criterion for Ignition Exceeded in an Inertial Fusion Experiment, *Phys. Rev. Lett.* **129**, 075001 (2022).
 - [17] A. L. Kritcher *et al.*, Design of an inertial fusion experiment exceeding the Lawson criterion for ignition, *Phys. Rev. E* **106**, 025201 (2022).
 - [18] A. B. Zylstra *et al.*, Experimental achievement and signatures of ignition at the National Ignition Facility, *Phys. Rev. E* **106**, 025202 (2022).
 - [19] C. A. Thomas, BigFoot, a program to reduce risk for indirect drive laser fusion, *Bull. Am. Phys. Soc.* **61**, 224 (2016).
 - [20] K. L. Baker *et al.*, High-Performance Indirect-Drive Cryogenic Implosions at High Adiabat on the National Ignition Facility, *Phys. Rev. Lett.* **121**, 135001 (2018).
 - [21] D. T. Casey *et al.*, The high velocity, high adiabat, ‘Bigfoot’ campaign and tests of indirect-drive implosion scaling, *Phys. Plasmas* **25**, 056308 (2018).

- [22] S. W. Haan *et al.*, Point design targets, specifications, and requirements for the 2010 ignition campaign on the National Ignition Facility, *Phys. Plasmas* **18**, 051001 (2011).
- [23] B. M. Haines *et al.*, Robustness to hydrodynamic instabilities in indirectly driven layered capsule implosions, *Phys. Plasmas* **26**, 012707 (2019).
- [24] B. M. Haines *et al.*, A mechanism for reduced compression in indirectly driven layered capsule implosions, *Phys. Plasmas* **29**, 042704 (2022).
- [25] M. M. Marinak *et al.*, Three-dimensional HYDRA simulations of National Ignition Facility targets, *Phys. Plasmas* **8**, 2275 (2001).
- [26] S. J. Ali *et al.*, Probing the seeding of hydrodynamic instabilities from nonuniformities in ablator materials using 2D velocimetry, *Phys. Plasmas* **25**, 092708 (2018).
- [27] V. A. Smalyuk *et al.*, Review of hydrodynamic instability experiments in inertially confined fusion implosions on National Ignition Facility, *Plasma Phys. Control. Fusion* **62**, 014007 (2019).
- [28] C. Weber, Understanding the impact of ablator micro-structure and fuel-ablator mixing on ICF implosions, *Bull. Am. Phys. Soc.* **64** (2019).
- [29] S. Davidovits, C. R. Weber, and D. S. Clark, Modeling and fuel-ablator mixing dynamics for perturbations driven by small-scale ablator inhomogeneity (unpublished).
- [30] S. V. Weber *et al.*, Simulations of indirectly driven gas-filled capsules at the National Ignition Facility, *Phys. Plasmas* (1994-present) **21**, 112706 (2014).
- [31] G. Dimonte and R. Tipton, K-L turbulence model for the self-similar growth of the Rayleigh-Taylor and Richtmyer-Meshkov instabilities, *Phys. Fluids* **18**, 085101 (2006).
- [32] D. Besnard, F. H. Harlow, R. M. Rauenzahn, and C. Zemach, Turbulent transport equations for variable-density turbulence and their relationship to two-field models (Los Alamos National Laboratory, LA-12303-MA, 1992) (online), available: <http://library.lanl.gov/cgi-bin/getfile?00193523.pdf>.
- [33] B. E. Morgan, O. Schilling, and T. A. Hartland, Two-length-scale turbulence model for self-similar buoyancy-, shock-, and shear-driven mixing, *Phys. Rev. E* **97**, 013104 (2018).
- [34] Y. Zhou, G. B. Zimmerman, and E. W. Burke, Formulation of a two-scale transport scheme for the turbulent mix induced by Rayleigh-Taylor and Richtmyer-Meshkov instabilities, *Phys. Rev. E* **65**, 056303 (2002).
- [35] G. Dimonte, Spanwise homogeneous buoyancy-drag model for Rayleigh-Taylor mixing and experimental evaluation, *Phys. Plasmas* **7**, 2255 (2000).
- [36] B. Bachmann *et al.*, Measurement of Dark Ice-Ablator Mix in Inertial Confinement Fusion, *Phys. Rev. Lett.* **129**, 275001 (2022).
- [37] Lord Rayleigh, *Investigation of the Character of the Equilibrium of an Incompressible Heavy Fluid of Variable Density*, Vol. s1-14 (1882) (online). Available: <http://plms.oxfordjournals.org>.
- [38] G. Taylor, *The Instability of Liquid Surfaces when Accelerated in a Direction Perpendicular to their Planes. I*, Vol. 201 (The Royal Society, 1950) (online). Available: <http://www.jstor.org/stable/98398>.
- [39] Y. Zhou, Rayleigh-Taylor and Richtmyer-Meshkov instability induced flow, turbulence, and mixing. I, *Phys. Rep.* **720-722**, 1 (2017).
- [40] Y. Zhou, Rayleigh-Taylor and Richtmyer-Meshkov instability induced flow, turbulence, and mixing. II, *Phys. Rep.* **723-725**, 1 (2017).
- [41] R. D. Richtmyer, Taylor instability in shock acceleration of compressible fluids, *Commun. Pure Appl. Math.* **13**, 297 (1960).
- [42] E. E. Meshkov, Instability of a shock wave accelerated interface between two gases, NASA Technical Translation **13**, 1 (1970).
- [43] V. N. Goncharov, P. McKenty, S. Skupsky, R. Betti, R. L. McCrory, and C. Cherfils-Clérouin, Modeling hydrodynamic instabilities in inertial confinement fusion targets, *Phys. Plasmas* **7**, 5118 (2000).
- [44] G. Dimonte, P. Ramaprabhu, and M. Andrews, Rayleigh-Taylor instability with complex acceleration history, *Phys. Rev. E* **76**, 046313 (2007).
- [45] G. Dimonte and M. Schneider, Density ratio dependence of Rayleigh-Taylor mixing for sustained and impulsive acceleration histories, *Phys. Fluids* **12**, 304 (2000).
- [46] J. Ding, T. Si, J. Yang, X. Lu, Z. Zhai, and X. Luo, Measurement of a Richtmyer-Meshkov Instability at an Air-SF₆ Interface in a Semiannular Shock Tube, *Phys. Rev. Lett.* **119**, 014501 (2017).
- [47] X. Luo *et al.*, Long-term effect of Rayleigh-Taylor stabilization on converging Richtmyer-Meshkov instability, *J. Fluid Mech.* **849**, 231 (2018).
- [48] F. Chen, A. Xu, and G. Zhang, Collaboration and competition between Richtmyer-Meshkov instability and Rayleigh-Taylor instability, *Phys. Fluids* **30**, 102105 (2018).
- [49] M. Vandenboomgaerde, C. Mügler, and S. Gauthier, Impulsive model for the Richtmyer-Meshkov instability, *Phys. Rev. E* **58**, 1874 (1998).
- [50] M. Lombardini, D. I. Pullin, and D. I. Meiron, Turbulent mixing driven by spherical implosions. Part 1. Flow description and mixing-layer growth, *J. Fluid Mech.* **748**, 85 (2014).
- [51] M. Flaig, D. Clark, C. Weber, D. L. Youngs, and B. Thornber, Single-mode perturbation growth in an idealized spherical implosion, *J. Comput. Phys.* **371**, 801 (2018).
- [52] N. J. Zabusky, J. Ray, and R. Samtaney, Vortex models for Richtmyer-Meshkov fast/slow environments: Scaling laws for interface growth rates, in *Proceedings of the Fifth International Workshop on Compressible Turbulent Mixing*, Stony Brook (1996) (online), available: http://www.iwpctm.org/proceedings/IWPCTM5/papers/Zabusky_Ray_Samtaney.pdf.
- [53] L. A. Pickworth *et al.*, Development of new platforms for hydrodynamic instability and asymmetry measurements in deceleration phase of indirectly driven implosions on NIF, *Phys. Plasmas* **25**, 082705 (2018).
- [54] A. L. Velikovich *et al.*, Multi-mode hydrodynamic evolution of perturbations seeded by isolated surface defects, *Phys. Plasmas* **27**, 102706 (2020).
- [55] U. Alon, J. Hecht, D. Ofer, and D. Shvarts, Power Laws and Similarity of Rayleigh-Taylor and Richtmyer-Meshkov Mixing Fronts at All Density Ratios, *Phys. Rev. Lett.* **74**, 534 (1995).
- [56] D. Ofer, U. Alon, D. Shvarts, R. L. McCrory, and C. P. Verdon, Modal model for the nonlinear multimode Rayleigh-Taylor instability, *Phys. Plasmas* **3**, 3073 (1996).
- [57] A. W. Cook and P. E. Dimotakis, Transition stages of Rayleigh-Taylor instability between miscible fluids, *J. Fluid Mech.* **443**, 69 (2001).

- [58] J. R. Ristorcelli and T. T. Clark, Rayleigh Taylor turbulence: Self-similar analysis and direct numerical simulations, *J. Fluid Mech.* **507**, 213 (2004).
- [59] J. H. Eggert *et al.*, Melting temperature of diamond at ultrahigh pressure, *Nat. Phys.* **6**, 40 (2010).
- [60] D. S. Clark *et al.*, Exploring implosion designs for increased compression on the National Ignition Facility using high density carbon ablaters, *Phys. Plasmas* **29**, 052710 (2022).
- [61] A. Do, C. R. Weber, E. L. Dewald, D. T. Casey, D. S. Clark, S. F. Khan, O. L. Landen, A. G. MacPhee, and V. A. Smalyuk, Direct Measurement of Ice-Ablator Interface Motion for Instability Mitigation in Indirect Drive ICF Implosions, *Phys. Rev. Lett.* **129**, 215003 (2022).
- [62] R. Tommasini *et al.*, Increased compression in HDC-based ablator implosions using modified dopant and drive profile (unpublished).